

1 **Evidence for the 3D radiative effects of boundary-layer**
2 **clouds from observations of direct and diffuse surface**
3 **solar fluxes**

4 **Najda Villefranque¹, Robin J. Hogan²**

5 ¹LMD-IPSL, Sorbonne University, CNRS, 4 pl Jussieu, Paris, France
6 ²ECMWF, Reading, United Kingdom

7 **Key Points:**

- 8 • Observed direct–diffuse partition of surface solar radiative fluxes is compared to
9 1D and 3D radiation calculations performed with ecRad
10 • Only the radiative transfer solver that includes 3D effects (SPARTACUS) is able
11 to reproduce the observations at large solar zenith angles
12 • Direct–diffuse partition is mostly sensitive to cloud cover, solar zenith angle, liq-
13 uid water content, cloud size and effective radius

Corresponding author: Najda Villefranque, najda.villefranque@lmd.ipsl.fr

This article has been accepted for publication and undergone full peer review but has not been through the copyediting, typesetting, pagination and proofreading process, which may lead to differences between this version and the [Version of Record](#). Please cite this article as [doi: 10.1029/2021GL093369](https://doi.org/10.1029/2021GL093369).

This article is protected by copyright. All rights reserved.

Abstract

Numerical experiments have revealed the importance of horizontal transport of light in the presence of clouds (“3D effects”), with consequences for climate, weather and solar resource availability predictions. Yet, analysis of 3D effects from observations remain sparse because of the difficulty to isolate the effect of horizontal transport in radiation measurements. In this paper, we provide observational evidence for 3D effects based on the direct–diffuse partition of surface solar fluxes. It is compared to outputs from the ecRad radiative transfer scheme run on retrieved cloud profiles. The direct-beam calculation takes careful account of the field-of-view of the pyrheliometer to ensure consistency between observed and modeled direct fluxes. Only the solver that accounts for 3D effects is able to reproduce the observed mean direct–diffuse partition as a function of solar zenith angle and cloud cover, in particular at large solar zenith angles where cloud sides intercept most of the direct beam.

Plain Language Summary

Accurately predicting the amount of solar energy that reaches the surface is of crucial importance for future climate projections and weather forecast, as well as for the solar energy industry. Atmospheric models include radiative transfer schemes, which are numerical models that represent the physical processes involved in the propagation of solar radiation. Understanding and modeling the impact of low-level clouds on solar radiation can be particularly challenging due to their frequent complex geometry. In this study, we provide observational evidence for the “3D radiative effects of clouds”, which are mostly due to the fact that cloud sides intercept the direct solar beam when the sun is low in the sky. To achieve this, we compare observations of surface radiation with outputs from numerical models that do and do not include a representation of 3D effects. We find good agreement between observed and modeled radiation on average only if 3D effects are taken into account in the radiative transfer scheme. Cloud 3D radiative effects are entirely missing from current atmospheric models; our results support the argument that they should be included. The radiative transfer scheme we use appears to be a promising candidate for future use in weather and climate models.

1 Introduction

Accurate predictions of the amount of solar radiation that reaches the surface under diverse atmospheric conditions are needed for various sensitive applications such as simulation of climate change, weather forecasts, and design and control of solar energy systems (see e.g. Lopes et al. (2018) and references therein). Boundary-layer clouds in particular have a major impact on solar surface radiation at different scales as they cover a large fraction of the Earth’s continents and oceans during most of the time and are optically thick to sunlight (Berg et al., 2011; Burleyson et al., 2015).

Radiative transfer parameterizations that are used in large-scale models to predict the solar radiative effect of clouds neglect 3D effects that are due to horizontal propagation of light. Long-standing efforts have been made to characterize 3D effects and understand the physical processes that drive them (e.g. McKee and Cox (1974); Várnai and Davies (1999)), their dependency on the cloud-field properties (e.g. Hinkelman et al. (2007)) and their potential impacts on microphysics and macrophysics (e.g. Jakub and Mayer (2017)). An important and complementary aspect is the development of 3D parameterizations for both large-scale (e.g. the SPEedy Algorithm for Radiative TrAnSfer through CloUd Sides (SPARTACUS); Hogan and Shonk (2013); Hogan et al. (2016, 2019)) and cloud-resolving models (e.g. the ten-stream model; (Jakub & Mayer, 2015)).

All these studies rely on numerical experiments; evidence of 3D effects in surface observations have remained elusive. Recently, Gristey et al. (2020b) have provided such

63 observational evidence by demonstrating that the bimodality characteristic of the dis-
64 tribution (PDF) of surface solar irradiance observed under cumulus cloud fields is a sig-
65 nature of the 3D radiative effects of clouds. They used high-resolution cloud fields from
66 Large-Eddy Simulations and Monte Carlo models to compare PDFs obtained from 1D
67 and 3D simulations to PDFs obtained from observations, and found that only 3D com-
68 putations can reproduce the PDF shape. They also show that 3D effects always increase
69 the diffuse flux component at the surface — which they explain by entrapment of light
70 through non-vertical reflections and diffuse radiation escaping from cloud sides — and
71 that they most often decrease the direct flux component, which they explain by inter-
72 ception of direct light by cloud sides. They suggest that taking these effects into account
73 in surface radiation forecasts might be particularly important for the solar energy indus-
74 try.

75 While many other arguments can be found in the literature in favor of atmospheric
76 models using 3D radiative transfer (RT) schemes instead of remaining with the 1D paradigm,
77 the resulting cost–benefit balance remains to be weighted for models at different scales.
78 For example, it is unknown how much representing 3D effects in long-term climate sim-
79 ulations might affect cloud properties, either directly through the feedback of surface fluxes
80 and heating rates on atmospheric processes or through the cloud parameter values se-
81 lected during the tuning process, in which cloud–radiation interactions play an impor-
82 tant role (Hourdin et al., 2017). The development of SPARTACUS, a 3D RT param-
83 eterization that is fast enough to be used in global simulations (at least for research pur-
84 poses) is an important element in this landscape. However, its use in climate simulations
85 should be accompanied by a thorough evaluation of its capacity to represent 3D cloud–
86 radiation interactions and a rigorous quantification of related uncertainties. Previous stud-
87 ies have shown reasonably good agreement between SPARTACUS and 3D RT models
88 run of detailed 3D cloud fields output from high-resolution atmospheric models (Hogan
89 et al., 2016, 2019; Villefranque et al., 2021). However, process-based evaluation of the
90 cloud part of a RT scheme using radiation observations remains difficult because the 3D
91 clouds above measured radiative fluxes are often insufficiently constrained.

92 In this paper, boundary-layer cloud vertical profiles retrieved from observations at
93 the ARM Graciosa site and processed by the Cloudnet analysis system (Illingworth et
94 al., 2007) are ingested by two versions of the ecRad radiation scheme (Hogan & Bozzo,
95 2018): one that includes 3D effects (SPARTACUS) and one that does not (Tripleclouds;
96 Shonk and Hogan (2008)). Ratios of direct to total surface solar fluxes (DTRs) obtained
97 from parameterized 1D and 3D computations are compared to DTRs computed from ARM
98 measurements, as a function of cloud cover and solar zenith angle. Sensitivity analysis
99 are performed to assess the relative importance of input data, model parameters and 3D
100 effects in the average accuracy of the DTR predictions.

101 Through our analysis, we provide:

- 102 • observational evidence of 3D radiative effects of clouds in the ratio of direct to to-
103 tal solar surface fluxes (DTR). While Gristey et al. (2020b) based their conclu-
104 sions on the analysis of a few high-resolution 3D cloud fields, ours are rather based
105 on long-term datasets of horizontally integrated cloud and radiation measurements;
- 106 • observation-based statistical validation of the solar component of SPARTACUS
107 in the presence of boundary-layer clouds.

108 The remainder of the manuscript is organized as follows. Section 2 describes the
109 ARM and Cloudnet data, the ecRad model and the methodology that is used to ana-
110 lyze the DTRs. Section 3 presents the resulting observed, 1D and 3D DTRs as a func-
111 tion of cloud cover and solar zenith angle, as well as a sensitivity analysis on various model
112 parameters. Finally, some implications of our findings are discussed in Section 4.

2 Method

The radiation observations used in this study consist of hourly averaged direct and total surface downwelling solar fluxes measured at the Graciosa island in the Azores archipelago. A first dataset, referred to as D1, consists of 19 months of hourly data from 5th June 2009 to 31st December 2010 and a second dataset (D2) consists of 26 months of hourly data from 17th July 2015 to 21st September 2017. Observations of downwelling solar radiation at the surface were taken from the Atmospheric Radiation Measurement (ARM) data (Atmospheric Radiation Measurement (ARM) user facility, 2009a, 2013a). The first dataset D1 corresponds to the data acquired by the ARM Mobile Facility deployed during the Clouds, Aerosol and Precipitation in the Marine Boundary Layer (CAP-MBL) campaign (Wood et al., 2015), and D2 corresponds to measurements acquired by the permanent observatory installed in 2013. Hourly-averaged broadband direct and total solar downwelling fluxes measured at the surface are used to compute the direct-to-total flux ratio (DTR). The direct flux is measured by a pyrheliometer characterized by a field-of-view of 5.7° . The total hemispheric flux is measured by a pyranometer. Only low clouds are considered in this study: cloud profiles where the maximum cloud fraction above 2500 meters is larger than 5% are excluded.

Rather than studying individual cases, DTRs are analyzed statistically, by averaging in bins of cloud cover and solar zenith angle (SZA). Both direct and total fluxes decrease when either cloud cover or SZA increases, but they do not decrease at the same rate, hence DTRs are also sensitive to cloud cover and SZA. For each hour, the observed DTR is associated with the corresponding hourly averaged SZA value and with the hourly averaged cloud cover value provided by the ARM Total Sky Imager (Atmospheric Radiation Measurement (ARM) user facility, 2009b, 2013b). The DTR is then attributed to one of five cloud-cover sub-intervals ($[0.1-0.3]$, $[0.3-0.5]$, $[0.5-0.7]$, $[0.7-0.9]$, $[0.9-1]$), and to one of nine SZA sub-intervals (obtained from applying the inverse cosine function to a regular division of the $[0.05-1]$ interval). The DTRs are averaged within each 2D bin and the associated 95% confidence interval width is computed in each bin as 1.96 times the standard deviation of the data divided by the square root of the number of independent samples in the bin. Samples are independent if they are separated by at least six hours of time, following Hogan et al. (2009) who found that this is the approximate e-folding time for cloud occurrence autocorrelation in cloud radar data.

Observed boundary-layer clouds coincident with observed radiation are then used as inputs to ecRad to compute 1D and 3D DTRs. Cloud fraction, mean liquid water content (LWC) and horizontal standard deviation of LWC (FSD) profiles are taken from the Cloudnet analysis system (Illingworth et al., 2007), which uses the same ARM measurements and provides retrievals averaged onto the grid of the ECMWF Integrated Forecasting System (IFS). Only the D1 dataset is used as the liquid water path available in D2 Cloudnet products appeared to be unreliable at the time of the analysis. Cloud fraction profiles at the resolution of the model are computed from high resolution (60 meters, 30 seconds) target categorization profiles based on lidar backscatter, radar reflectivity and Doppler velocity. The cloud cover is also diagnosed from the high-resolution categorization profiles, as the fraction of profiles containing clouds in each period of one hour. LWC profiles are computed following the scaled adiabatic method: the adiabatic liquid water content is calculated from temperature in each separate cloud layer from cloud base derived from the Micro Pulse Lidar to cloud top derived from the profiling radar. Then the LWC values are scaled to match the liquid water path (LWP) as inferred from microwave radiometer measurements. Data including precipitation at the surface are excluded because of unreliable LWP measurements. Profiles of mean LWC and standard deviation of non-zero LWC are then computed at each hour. Figure 1(a) and (b) present 72-hours-long timeseries of LWC and cloud fraction profiles for illustration. In order to exclude profiles where high clouds are present, hours when the maximum observed cloud fraction above 2500 m is greater than 5% are filtered out. Temperature, pres-

166 sure, water vapour content and ozone concentration are taken from the IFS high-resolution
167 forecast at the gridpoint closest to Graciosa Island, and aerosol and trace gas concen-
168 trations are taken from the same climatology as the IFS. Two sensitivity tests are per-
169 formed to assess the uncertainty related to the Cloudnet retrievals, one with FSD=0.75
170 (Shonk et al., 2010) and one using LWC profiles scaled by 1.5.

171 Other cloud parameters that could not be directly derived from local observations
172 are set according to the literature, yielding a reference configuration. Sensitivity tests
173 are performed for each parameter separately (in each sensitivity test, all other param-
174 eters are kept to their reference values). The effective radius of liquid droplets r_e is set
175 to 8.2 μm in the reference configuration, according to aircraft data collected in maritime
176 clouds during the ASTEX campaign (Yum & Hudson, 2002). A sensitivity test is per-
177 formed using $r_e = 12.4 \mu\text{m}$, which is the average value reported by Dong et al. (2014),
178 based on retrievals from LWP and solar radiation observations in Graciosa single-layered
179 clouds during the CAP-MBL campaign. The overlap decorrelation length z_0 that appears
180 in the exponential-random overlap scheme used in Tripleclouds and SPARTACUS is set
181 to 2000 m in the reference configuration and 1000 m in the sensitivity test (Barker, 2008;
182 Hogan & Illingworth, 2000). The cloud-edge length that is needed in SPARTACUS is
183 parameterized as a function of cloud fraction and an effective cloud spacing parameter
184 C_x , set to 2000 m in the reference configuration and 1000 m in the sensitivity test, fol-
185 lowing Fielding et al. (2020). The surface albedo α is set to 15% in the reference con-
186 figuration to represent the radiative effect of the surface in a 2-km radius circle around
187 the observatory. It is a weighted average of the sea value (around 6%) and the locally
188 observed value, around 20% (on average, computed from the ratio of upward to down-
189 ward flux at the surface, not shown), in which slightly more land is accounted for. A sen-
190 sitivity test is performed with $\alpha = 7.5\%$.

191 Modeled DTRs are computed using the ecRad radiation scheme (Hogan & Bozzo,
192 2018). Radiative transfer is solved using variants of a two-stream model. In the 1D solver
193 Tripleclouds (Shonk & Hogan, 2008), the two-stream equations are modified to repre-
194 sent cloud geometry effects due to layers being only partially occupied by clouds, the de-
195 gree of vertical overlap of the cloudy regions in different layers, and in-cloud liquid wa-
196 ter content variability. In the 3D solver SPARTACUS (Schäfer et al., 2016; Hogan et al.,
197 2016, 2019), terms are added to the Tripleclouds scheme to represent the effects of hor-
198 izontal transport of light: photons escaping through cloud sides, entrapment of light due
199 to non-vertical reflections, and interception of direct light by cloud sides when the sun
200 is not at zenith. For a given cloud fraction, the intensity of these effects increases with
201 the number of clouds: more clouds means a larger area of cloud sides through which ra-
202 diation can flow. The output DTRs are binned according to the cloud cover value di-
203 agnosed by ecRad, which depends on the input Cloudnet cloud fraction profile and on
204 the vertical overlap assumptions. Note that the cloud cover estimates used to bin the
205 modeled and observed DTRs are inconsistent with each other but consistent with the
206 nature of the DTR: observed DTRs were computed from radiation measurements that
207 have “seen” the whole sky thus they are associated with hemispheric cloud covers diag-
208 nosed by the TSI, while modeled DTRs were computed from simulated radiation that
209 has only “seen” vertical profiles thus they are associated with cloud covers derived from
210 these profiles.

211 To be able to compare observed and modeled DTRs, the definition of direct flux
212 should be the same in the two worlds. The pyrhelimeter measures radiation incident
213 into a normal plane to the sun direction and into a small solid angle around the sun di-
214 rection. However, most radiation schemes, including ecRad, rely on the delta-Eddington
215 approximation of Joseph et al. (1976), which treats a fraction f of the forward-scattered
216 radiation as if it had not been scattered at all, thereby increasing the radiation treated
217 as “direct” to include more than purely unscattered radiation from the sun. In this ap-
218 proximation, optical properties are scaled to replace thick clouds characterized by strongly

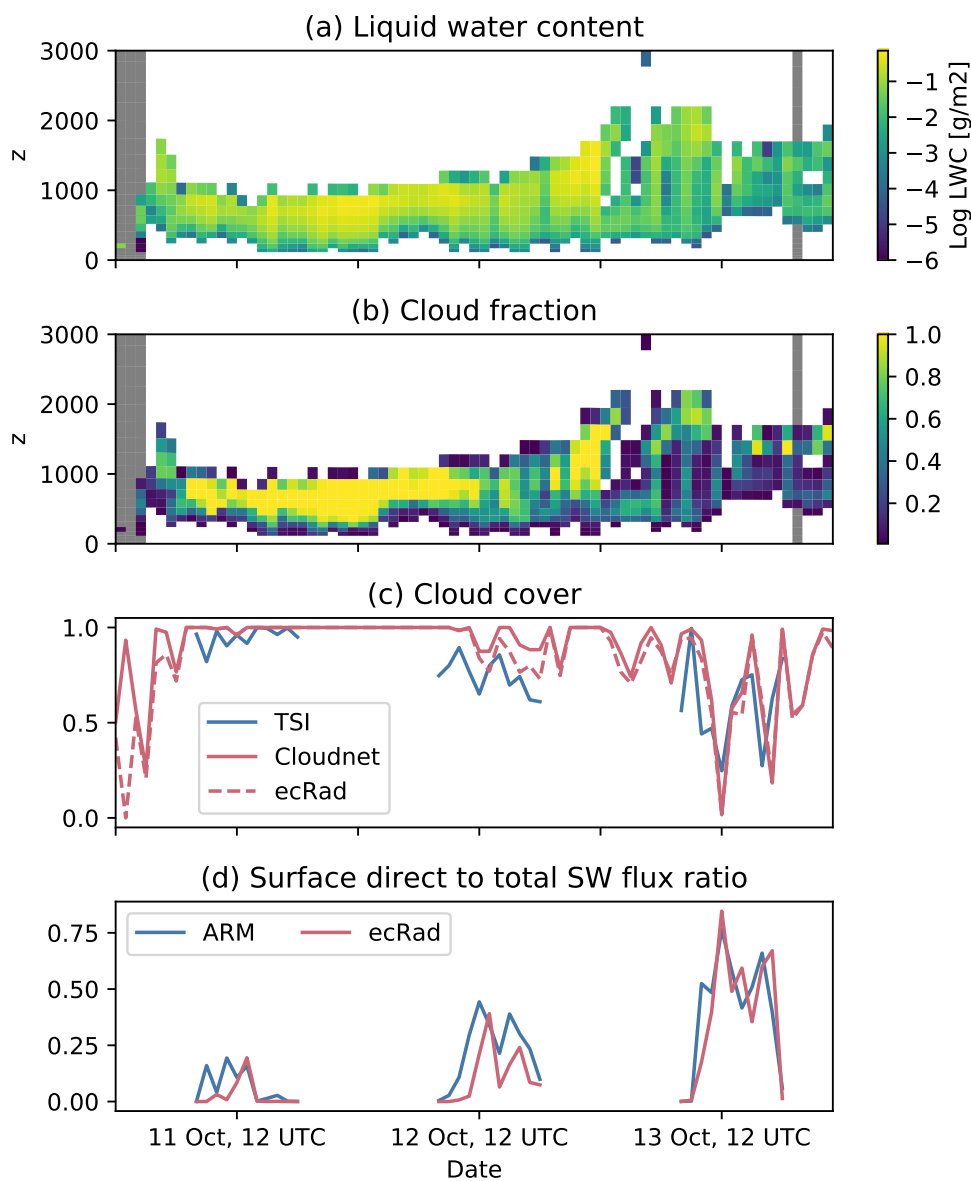


Figure 1. Timeseries of (a) Cloudnet liquid water content, (b) Cloudnet cloud fraction profiles, (c) cloud cover diagnosed by the Total Sky Imager (TSI), from Cloudnet categorization profiles and by ecRad using the Cloudnet cloud fraction profiles along with vertical overlap assumptions, (d) DTRs in ARM observations and from ecRad using the SPARTACUS solver run on the Cloudnet cloud profiles. Gray shadings in (a) and (b) correspond to profiles where the maximum cloud fraction above 2500 m is greater than 5%, which were excluded from the analysis.

219 asymmetric phase functions that scatter most of the energy into a small forward solid angle,
 220 by optically thinner clouds with phase functions closer to isotropic. The resulting
 221 reduction of the attenuation of the direct beam is compensated by an increase of back-
 222 ward scattering. While this increases the accuracy of total flux estimates, the “direct”
 223 flux can no longer be compared directly to pyrheliometer measurements. To ensure con-
 224 sistency between the definition of the modeled direct flux and the flux seen by a pyrhe-
 225 liometer, Räisänen and Lindfors (2019) derived a parameterization for the delta-scaling
 226 factor that depends on the FOV angle of the instrument and on the effective radius of
 227 the liquid droplets or ice crystal size distribution. A slightly simpler approach was taken
 228 here, whereby the delta-Eddington factor is scaled by a further value β , that is then as-
 229 sumed constant in ecRad calculations:

$$f_{corr} = \beta \times f_{Edd} \approx f_p$$

230 where $f_{Edd} = g^2$ is the delta-Eddington scaling factor (where the asymmetry factor, g ,
 231 is the average of the cosine of the scattering angle) and f_p is the fraction of energy that
 232 is scattered into a 2.85° forward angle (the half width of the field-of-view of the pyrhe-
 233 liometer). The computation of β uses detailed phase functions computed from the Mie
 234 theory, integrated over gamma size distributions parameterized by the effective radius
 235 $r_e = 10\mu m$ and various effective variances v_e (the same data underly the cloud optics
 236 parameterization SOCRATES used in ecRad; Manners et al. (2017)). This is shown in
 237 Figure 2. β is in fact a decreasing function of the wavelength and ranges from 0.61 to
 238 0.42 between 400 and 1600 nm (not shown). In the following, it is set uniformly to 0.6
 239 for the reference configuration, and sensitivity tests are performed with $\beta = 1$ and $\beta =$
 240 0.5. For each configuration, ecRad is called twice on each column: once with $f = f_{Edd}$
 241 to produce appropriate estimations of the total flux and once with $f = f_{corr}$ to produce
 242 appropriate estimations of the direct flux.

243 To measure the quality of a particular ecRad configuration compared to ARM mea-
 244 surements, an error metric is computed for each of the five cloud cover values \times nine so-
 245 lar zenith angle sub-intervals as:

$$I_m(c, \theta_0) = \frac{|\text{DTR}_{obs}(c, \theta_0) - \text{DTR}_m(c, \theta_0)|}{\sqrt{\sigma_{obs}(c, \theta_0)^2 + \sigma_m(c, \theta_0)^2}} \quad (1)$$

246 where m is the model configuration, (c, θ_0) the cloud cover \times solar zenith angle sub-interval,
 247 $\text{DTR}_{obs}(c, \theta_0)$ is the ARM mean DTR in the (c, θ_0) sub-interval, $\text{DTR}_m(c, \theta_0)$ is the mean
 248 DTR predicted by ecRad configuration m in (c, θ_0) and $\sigma_{obs}(c, \theta_0)$ (respectively $\sigma_m(c, \theta_0)$)
 249 is the standard deviation associated with $\text{DTR}_{obs}(c, \theta_0)$ (respectively, $\text{DTR}_m(c, \theta_0)$). The
 250 normalization is a way to account for the uncertainties due to internal variability and
 251 limited sampling within the sub-intervals. If $I_m(c, \theta_0) < 1$, it means the model error
 252 is dominated by the statistical uncertainty associated with the averaging method. Oth-
 253 erwise, the model–observation distance becomes significant. To summarize the error over
 254 all the (c, θ_0) bins, two metrics are used:

$$I_{m,max} = \max_{(c, \theta_0)} \{I_m(c, \theta_0)\} \quad \text{and} \quad I_{m,L2} = \sqrt{\sum_{(c, \theta_0)} I_m(c, \theta_0)^2} \quad (2)$$

255 3 Results

256 The observed and modeled direct-to-total fluxes ratios (DTRs) are shown in Fig-
 257 ure 3 as a function of cloud cover and SZA. Observational data cover the 2009-2010 (D1)
 258 and 2015-2017 (D2) time periods while modeled DTRs only include data from D1. Both
 259 modeled and observed data show that the average DTR decreases with increasing cloud
 260 cover because the direct flux decreases more rapidly than the total flux. Both modeled
 261 and observed data show that average DTRs also decrease with increasing SZA. The mech-
 262 anism for this in the 1D case represented by Tripleclouds is the increased path length

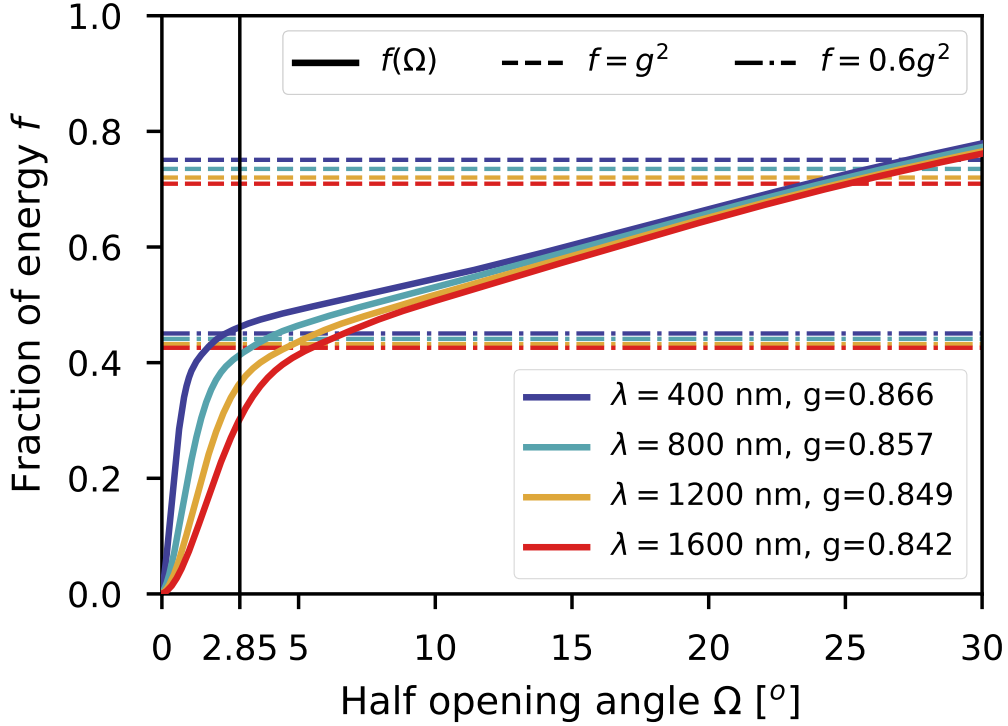


Figure 2. Fraction f of radiation scattered by liquid droplets (y-axis) in a forward half-angle of aperture Ω , computed from Mie phase functions integrated over gamma size distributions with effective radius $r_e = 10 \mu\text{m}$ and varying effective variances (see text) for four wavelengths over the visible and near-infrared spectrum. Solid lines give f as a function of Ω ; dashed lines correspond to values of f that are used in the δ -Eddington approximation ($f = f_{Edd} = g^2$ where g is the phase function asymmetry parameter); point-dashed lines correspond to $f = f_{corr} = \beta \times f_{Edd}$ with $\beta = 0.6$. The vertical black line corresponds to the half angle of the field-of-view of the ARM pyrheliosimeter.

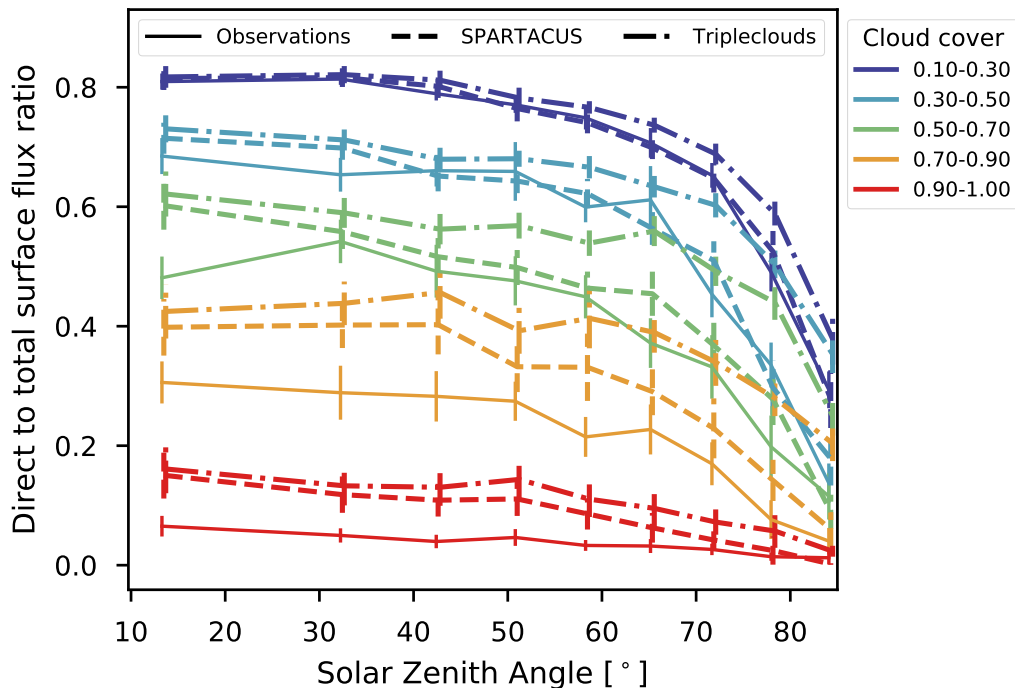


Figure 3. Average direct-to-total ratio of solar surface fluxes as a function of solar zenith angle. The solar zenith angle was discretized into nine sub-intervals. Colors correspond to five different cloud cover intervals. Solid lines correspond to observations, dashed lines correspond to ecRad outputs using the SPARTACUS 3D solver, point-dashed lines correspond to ecRad outputs using the Tripleclouds 1D solver. Error bars indicate the 95% confidence interval around the average value.

263 through the atmosphere leading to more rapid attenuation of the direct beam when the
 264 sun is lower in the sky. The speed of decrease is highly sensitive to the representation
 265 of 3D effects: neglecting these effects leads to inaccurate dependency of the DTR to the
 266 SZA, while taking them into account leads to good agreement between modeled and ob-
 267 served DTRs. Indeed, both direct and diffuse fluxes are modified by 3D effects: they de-
 268 crease the direct surface flux by enhancing the interception of the direct beam by cloud
 269 sides and they increase the diffuse surface flux by enhancing cloud side reflection and en-
 270 trapment. Both effects lead to a decrease of DTR when the intensity of 3D effects in-
 271 creases, i.e. when the sun approaches the horizon. Representing 3D effects is crucial to
 272 reproduce the rate of decrease of DTRs with solar angle. Discrepancies remain between
 273 modeled and observed DTRs for small SZAs at large cloud covers. Since this behaviour
 274 was not evidenced in previous studies comparing SPARTACUS to 3D RT models when
 275 cloud fields were perfectly known (e.g. Hogan et al. (2019)), it is probable that uncer-
 276 tain cloud and radiation parameters are first responsible for these discrepancies rather
 277 than the misrepresentation of an important process in the SPARTACUS scheme itself,
 278 although this remains to be demonstrated. However, the disagreement in the [0.9–1] cloud
 279 cover bin demonstrates that this discrepancy is not likely to be due to 3D effects.

280 Sensitivity tests were performed to analyze the dependency of DTRs to various cloud
 281 characteristics, quantify the relative importance of 3D effects on the DTR estimates and
 282 probe the increase in SPARTACUS DTR estimates accuracy that could be gained by finer

283 tuning of free parameters. For each configuration, the two errors metrics $I_{m,max}$ and $I_{m,L2}$
284 are shown in Figure 4. Comparing $I_{m,max}$ and $I_{m,L2}$ for 1D and 3D ecRad configurations
285 shows that 3D effects are a key ingredient to significantly reduce the distance between
286 the observed and modeled DTRs. The other parameters that most affect the DTRs and
287 might explain the remaining discrepancies between observations and model outputs seen
288 in Figure 3 are: the liquid water content (LWC) and its fractional standard deviation
289 (FSD), which might be biased in the retrievals; the effective radius r_e which was set to
290 a constant value instead of a function of LWC; the cloud spacing parameter C_x that con-
291 trols the intensity of 3D effects; and the β factor that was applied to correct delta-scaling,
292 which drastically modifies the estimate of direct flux. Surface albedo and overlap param-
293 eters have small impact: doubling the surface albedo only slightly increases the total down-
294 ward flux at the surface, while changing the overlap parameter both changes radiation
295 and cloud cover and hence preserves the average DTR computed over a given cloud cover
296 sub-interval. These results agree with previous studies, for instance similar parameters
297 were found to explain the PDF of surface solar irradiance under 3D cumulus clouds us-
298 ing machine learning in Gristey et al. (2020a). Note however that since the extent to which
299 the different parameters were perturbed is not uniform, their relative importance was
300 not thoroughly quantified here.

301 4 Conclusions

302 In this paper, observations of the partition of solar surface fluxes into direct and
303 diffuse components have been analyzed. It was demonstrated that the dependency of the
304 DTR to solar zenith angle can only be reproduced by a radiative transfer scheme that
305 represents 3D effects. This is observational evidence for the 3D radiative effects of bound-
306 ary layer clouds. The SPARTACUS solver that was used to simulate sub-grid 3D prop-
307 agation of radiation produces accurate estimates of the DTRs on average. It implies that
308 SPARTACUS is treating 3D solar effects well, particularly the interception of the direct
309 beam by cloud sides, giving confidence to its potential future use in weather and climate
310 models.

311 The analysis was based on statistical comparisons rather than direct comparison
312 of time series. One of the main reasons is that cloud profiles provided as inputs to ecRad
313 are only a sub-sample of the 3D atmosphere that was “seen” during the same hour by
314 the radiation instruments. If the structure of the cloud field is not random then there
315 is no reason for the vertical profiles to be representative of the whole cloud field and the
316 associated radiation cannot be compared. Our statistical approach has other limitations:
317 uncertainties due for instance to the cloud cover estimate used to bin the measured DTRs
318 or to the limited amount of data. Further work should aim at reducing these uncertain-
319 ties for instance by adding newly acquired measurements.

320 The sensitivity of the DTRs to input data and parameters was also investigated.
321 Uncertainties in the retrieval of the profiles of cloud properties (such as the mean LWC
322 and its subgrid variability) or insufficiently constrained parameters (such as effective ra-
323 dius or cloud spacing) might explain discrepancies between SPARTACUS and the ob-
324 servations. This could be further investigated by an extensive sensitivity analysis in which
325 SPARTACUS parameter space would be thoroughly explored, for instance using the same
326 approach as in Villefranque et al. (2020).

327 Another point is that direct flux output from radiation models that use the delta-
328 Eddington approximation should not be compared directly to observations. Depending
329 on the application, predictions of the direct surface flux might need to be corrected to
330 ensure consistency between the size of the direct beam in the model and the one that
331 is relevant to the application. This issue was also raised by Sun et al. (2016) and Räisänen
332 and Lindfors (2019). The latter proposed a sophisticated parameterization to scale the
333 cloud optical properties as a function of the instrument field-of-view. Their parameter-

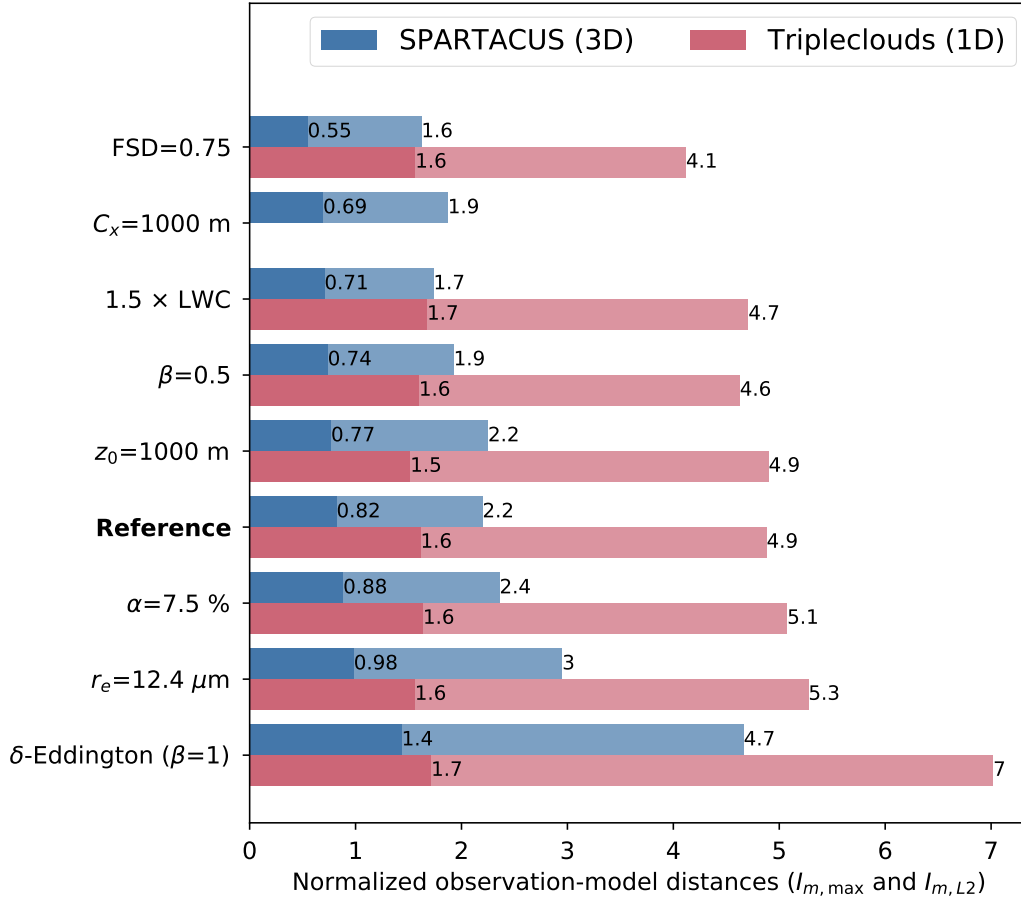


Figure 4. Maximum and L2 errors (see Equations 1 and 2) associated with different configurations of ecRad. The label on the y-axis indicates the change in configuration with respect to the “**Reference**” configuration, which is as follows: the liquid water content profile (LWC) and the fractional standard deviation of in-cloud liquid water (FSD) are taken from the Cloudnet retrievals, the delta-scaling correction factor $\beta=0.6$, the cloud spacing parameter $C_x = 2000$ m, the surface albedo $\alpha = 15\%$, the overlap decorrelation length $z_0 = 2000$ m, the effective radius $r_e = 7 \mu\text{m}$. Each bar gives the maximum (dark shading) and L2-norm (light shading) of errors computed over the five cloud cover values \times nine solar zenith angles sub-intervals (see text), with associated numbers given at the right side of each bar. Blue bars are associated with the SPARTACUS solver that accounts for 3D effects and red bars are associated with the Tripleclouds solver that neglects 3D effects. The C_x parameter is not used in Tripleclouds hence the missing red bar.

334 ization is an alternative to the delta-Eddington scaling factor of Joseph et al. (1976). Here,
 335 we propose another solution that consists in scaling the delta-Eddington factor by a cor-
 336 rection factor β , which was only appropriate because only liquid boundary-layer clouds
 337 with uniform effective radii were considered in this study.

338 This study provides observational support for the argument that 3D effects should
 339 be represented in large-scale models. Models need to provide accurate estimates of sur-
 340 face radiative fluxes to users, in particular to the actors of the solar energy industry who
 341 need this information to design systems and optimize their productivity — a major chal-
 342 lenge in the context of the large-scale energy transition that is urgently needed. The sta-
 343 tistical evidence of 3D radiative effects of clouds we found in surface observations also
 344 motivates the need to investigate their impact on climate sensitivity and global climate
 345 change.

346 Acknowledgments

347 N. V. was funded by the ERASMUS+ program and by l'École des Docteurs de Toulouse
 348 for her two-month visit at the ECMWF during her PhD studies. We thank Maike Ahlgrimm,
 349 Alessio Bozo, Mark Fielding and Ewan O'Connor for interesting discussions. We are grate-
 350 ful for the helpful work accomplished by two anonymous reviewers. N. V. thanks Fra-
 351 noise Guichard for her everlasting support and inspiring enthusiasm for observational
 352 datasets. The data used for this study is available under DOI:10.14768/2bfb2db9-f438-
 353 4937-a1fa-bac45b4db6f7.

354 References

- 355 Atmospheric Radiation Measurement (ARM) user facility. (2009a). *Data Quality*
 356 *Assessment for ARM Radiation Data (QCRAD1LONG). 2009-04-16 to 2011-*
 357 *01-06, ARM Mobile Facility (GRW) Graciosa Island, Azores, Portugal; AMF1*
 358 *(M1)*. Data set accessed 2019-07-01 at <http://dx.doi.org/10.5439/1227214>.
 359 (Compiled by D. Zhang and C. Long. ARM Data Center.)
- 360 Atmospheric Radiation Measurement (ARM) user facility. (2009b). *Total Sky Imager*
 361 *(TSISKYCOVER). 2009-04-14 to 2011-01-05, ARM Mobile Facility (GRW)*
 362 *Graciosa Island, Azores, Portugal; AMF1 (M1)*. Data set accessed 2019-07-01
 363 at <http://dx.doi.org/10.5439/1025308>. (Compiled by V. Morris and D. Flynn.
 364 ARM Data Center.)
- 365 Atmospheric Radiation Measurement (ARM) user facility. (2013a). *Data Quality*
 366 *Assessment for ARM Radiation Data (QCRAD1LONG) 2013-10-03 to 2019-*
 367 *10-17, Eastern North Atlantic (ENA) Graciosa Island, Azores, Portugal (C1)*.
 368 Data set accessed 2019-07-01 at <http://dx.doi.org/10.5439/1227214>. (Compiled
 369 by L. Riihimaki, Y. Shi, D. Zhang and C. Long. ARM Data Center.)
- 370 Atmospheric Radiation Measurement (ARM) user facility. (2013b). *Total Sky Im-*
 371 *ager (TSISKYCOVER). 2013-10-01 to 2021-03-10, Eastern North Atlantic*
 372 *(ENA) Graciosa Island, Azores, Portugal (C1)*. Data set accessed 2019-07-01
 373 at <http://dx.doi.org/10.5439/1025308>. (Compiled by V. Morris and D. Flynn.
 374 ARM Data Center.)
- 375 Barker, H. W. (2008). Overlap of fractional cloud for radiation calculations in gcm:
 376 A global analysis using cloudsat and calipso data. *Journal of Geophysical Re-*
 377 *search: Atmospheres*, 113(D8). doi: 10.1029/2007JD009677
- 378 Berg, L. K., Kassianov, E. I., Long, C. N., & Mills, D. L. (2011, January). Sur-
 379 face summertime radiative forcing by shallow cumuli at the Atmospheric
 380 Radiation Measurement Southern Great Plains site. *Journal of Geophys-*
 381 *ical Research-Atmospheres*, 116, D01202. (WOS:000286058200002) doi:
 382 10.1029/2010JD014593
- 383 Burleyson, C. D., Long, C. N., & Comstock, J. M. (2015). Quantifying Diurnal
 384 Cloud Radiative Effects by Cloud Type in the Tropical Western Pacific. *Jour-*

- 385 *nal of Applied Meteorology and Climatology*, 54(6), 1297 - 1312. doi: 10.1175/
386 JAMC-D-14-0288.1
- 387 Dong, X., Xi, B., Kennedy, A., Minnis, P., & Wood, R. (2014). A 19-Month Record
388 of Marine AerosolCloudRadiation Properties Derived from DOE ARM Mo-
389 bile Facility Deployment at the Azores. Part I: Cloud Fraction and Single-
390 Layered MBL Cloud Properties. *Journal of Climate*, 27(10), 3665 - 3682. doi:
391 10.1175/JCLI-D-13-00553.1
- 392 Fielding, M. D., Schfer, S. A. K., Hogan, R. J., & Forbes, R. M. (2020). Parametriz-
393 ing cloud geometry and its application in a subgrid cloud-edge erosion scheme.
394 *Quarterly Journal of the Royal Meteorological Society*, 146(729), 1651-1667.
395 doi: 10.1002/qj.3758
- 396 Gristey, J. J., Feingold, G., Glenn, I. B., Schmidt, K. S., & Chen, H. (2020a). On
397 the relationship between shallow cumulus cloud field properties and surface
398 solar irradiance. *Geophysical Research Letters*, 47(22), e2020GL090152. doi:
399 https://doi.org/10.1029/2020GL090152
- 400 Gristey, J. J., Feingold, G., Glenn, I. B., Schmidt, K. S., & Chen, H. (2020b). Sur-
401 face solar irradiance in continental shallow cumulus fields: Observations and
402 large-eddy simulation. *Journal of the Atmospheric Sciences*, 77(3), 1065 -
403 1080. doi: 10.1175/JAS-D-19-0261.1
- 404 Hinkelman, L. M., Evans, K. F., Clothiaux, E. E., Ackerman, T. P., & Stackhouse,
405 P. W. (2007). The effect of cumulus cloud field anisotropy on domain-averaged
406 solar fluxes and atmospheric heating rates. *Journal of the Atmospheric Sci-
407 ences*, 64(10), 3499-3520. doi: 10.1175/JAS4032.1
- 408 Hogan, R. J., & Bozzo, A. (2018). A flexible and efficient radiation scheme for the
409 ECMWF model. *Journal of Advances in Modeling Earth Systems*. doi: 10
410 .1029/2018MS001364
- 411 Hogan, R. J., Fielding, M. D., Barker, H. W., Villefranche, N., & Schfer, S. A. K.
412 (2019). Entrapment: An Important Mechanism to Explain the Shortwave
413 3D Radiative Effect of Clouds. *Journal of the Atmospheric Sciences*, 76(7),
414 2123-2141. doi: 10.1175/JAS-D-18-0366.1
- 415 Hogan, R. J., & Illingworth, A. J. (2000, October). Deriving cloud overlap statistics
416 from radar. *Quarterly Journal of the Royal Meteorological Society*, 126(569),
417 2903-2909. doi: 10.1002/qj.49712656914
- 418 Hogan, R. J., O'Connor, E. J., & Illingworth, A. J. (2009). Verification of cloud-
419 fraction forecasts. *Quarterly Journal of the Royal Meteorological Society*,
420 135(643), 1494-1511. doi: https://doi.org/10.1002/qj.481
- 421 Hogan, R. J., Schäfer, S. A. K., Klinger, C., Chiu, J. C., & Mayer, B. (2016, July).
422 Representing 3-D cloud radiation effects in two-stream schemes: 2. Matrix
423 formulation and broadband evaluation. *Journal of Geophysical Research:
424 Atmospheres*, 121(14), 2016JD024875. doi: 10.1002/2016JD024875
- 425 Hogan, R. J., & Shonk, J. K. P. (2013, February). Incorporating the Effects of 3d
426 Radiative Transfer in the Presence of Clouds into Two-Stream Multilayer Ra-
427 diation Schemes. *Journal of the Atmospheric Sciences*, 70(2), 708-724. doi:
428 10.1175/JAS-D-12-041.1
- 429 Hourdin, F., Mauritsen, T., Gettelman, A., Golaz, J.-C., Balaji, V., Duan, Q.,
430 ... Williamson, D. (2017). The art and science of climate model tun-
431 ing. *Bulletin of the American Meteorological Society*, 98(3), 589-602. doi:
432 10.1175/BAMS-D-15-00135.1
- 433 Illingworth, A. J., Hogan, R. J., O'connor, E. J., Bouniol, D., Delano, J., Pelon, J.,
434 ... others (2007). Cloudnet: Continuous evaluation of cloud profiles in seven
435 operational models using ground-based observations. *Bulletin of the American
436 Meteorological Society*, 88(6), 883-898.
- 437 Jakub, F., & Mayer, B. (2015, September). A three-dimensional parallel radiative
438 transfer model for atmospheric heating rates for use in cloud resolving model-
439 sThe TenStream solver. *Journal of Quantitative Spectroscopy and Radiative*

- 440 *Transfer*, 163, 63–71. doi: 10.1016/j.jqsrt.2015.05.003
- 441 Jakub, F., & Mayer, B. (2017, May). The Role of 1d and 3d Radiative Heating
442 on the Organization of Shallow Cumulus Convection and the Formation of
443 Cloud Streets. *Atmospheric Chemistry and Physics Discussions*, 1–16. doi:
444 10.5194/acp-2017-415
- 445 Joseph, J. H., Wiscombe, W. J., & Weinman, J. A. (1976, December). The Delta-
446 Eddington Approximation for Radiative Flux Transfer. *Journal of the Atmo-
447 spheric Sciences*, 33(12), 2452–2459. doi: 10.1175/1520-0469(1976)033<2452:
448 TDEAFR>2.0.CO;2
- 449 Lopes, F. M., Silva, H. G., Salgado, R., Cavaco, A., Canhoto, P., & Collares-Pereira,
450 M. (2018). Short-term forecasts of GHI and DNI for solar energy sys-
451 tems operation: assessment of the ECMWF integrated forecasting system
452 in southern Portugal. *Solar Energy*, 170, 14–30. doi: [https://doi.org/10.1016/
453 j.solener.2018.05.039](https://doi.org/10.1016/j.solener.2018.05.039)
- 454 Manners, J., Edwards, J. M., Hill, P., & Thelen, J.-C. (2017). *SOCRATES Tech-
455 nical Guide Suite Of Community RAdiative Transfer codes based on Edwards
456 and Slingo* (Tech. Rep.). FitzRoy Rd, Exeter EX1 3PB: Met Office. Re-
457 trieved from [http://homepages.see.leeds.ac.uk/~lecsjed/winscpuse/
458 socrates_techguide.pdf](http://homepages.see.leeds.ac.uk/~lecsjed/winscpuse/socrates_techguide.pdf)
- 459 McKee, T. B., & Cox, S. K. (1974). Scattering of Visible Radiation by Finite
460 Clouds. *Journal of the Atmospheric Sciences*, 31(7), 1885–1892. doi:
461 10.1175/1520-0469(1974)031<1885:SOVRBF>2.0.CO;2
- 462 Räisänen, P., & Lindfors, A. V. (2019). On the computation of apparent direct so-
463 lar radiation. *Journal of the Atmospheric Sciences*, 76(9), 2761–2780. doi: 10
464 .1175/JAS-D-19-0030.1
- 465 Schäfer, S. A. K., Hogan, R. J., Klinger, C., Chiu, J. C., & Mayer, B. (2016, July).
466 Representing 3-D cloud radiation effects in two-stream schemes: 1. Longwave
467 considerations and effective cloud edge length. *Journal of Geophysical Re-
468 search: Atmospheres*, 121(14), 2016JD024876. doi: 10.1002/2016JD024876
- 469 Shonk, J. K. P., & Hogan, R. J. (2008, june). Tripleclouds: An Efficient Method
470 for Representing Horizontal Cloud Inhomogeneity in 1d Radiation Schemes by
471 Using Three Regions at Each Height. *Journal of Climate*, 21(11), 2352–2370.
472 doi: 10.1175/2007JCLI1940.1
- 473 Shonk, J. K. P., Hogan, R. J., Edwards, J. M., & Mace, G. G. (2010, July). Effect
474 of improving representation of horizontal and vertical cloud structure on the
475 Earth’s global radiation budget. Part I: review and parametrization. *Quarterly
476 Journal of the Royal Meteorological Society*, n/a–n/a. doi: 10.1002/qj.647
- 477 Sun, Z., Li, J., He, Y., Li, J., Liu, A., & Zhang, F. (2016). Determination of di-
478 rect normal irradiance including circumsolar radiation in climate/nwp models.
479 *Quarterly Journal of the Royal Meteorological Society*, 142(700), 2591–2598.
480 doi: <https://doi.org/10.1002/qj.2848>
- 481 Várnai, T., & Davies, R. (1999). Effects of cloud heterogeneities on shortwave radi-
482 ation: Comparison of cloud-top variability and internal heterogeneity. *Journal
483 of the Atmospheric Sciences*, 56(24), 4206–4224.
- 484 Villefranque, N., Blanco, S., Couvreur, F., Fournier, R., Gautrais, J., Hogan, R. J.,
485 ... Williamson, D. (2021). Process-based climate model development har-
486 nassing machine learning: Iii. the representation of cumulus geometry and their
487 3d radiative effects. *Journal of Advances in Modeling Earth Systems*, 13(4),
488 e2020MS002423. doi: <https://doi.org/10.1029/2020MS002423>
- 489 Villefranque, N., Williamson, D., Couvreur, F., Hourdin, F., Gautrais, J., Fournier,
490 R., ... Volodina, V. (2020). Process-based climate model development har-
491 nassing machine learning: III. The Representation of Cumulus Geometry and
492 their 3D Radiative Effects. *Earth and Space Science Open Archive*, 30. Re-
493 trieved from <https://doi.org/10.1002/essoar.10505088.1> (Submitted to
494 JAMES) doi: 10.1002/essoar.10505088.1

- 495 Wood, R., Wyant, M., Bretherton, C. S., Rémillard, J., Kollias, P., Fletcher, J., ...
496 Lin, Y. (2015). Clouds, Aerosols, and Precipitation in the Marine Bound-
497 ary Layer: An Arm Mobile Facility Deployment. *Bulletin of the American*
498 *Meteorological Society*, 96(3), 419 - 440. doi: 10.1175/BAMS-D-13-00180.1
499 Yum, S. S., & Hudson, J. G. (2002). Maritime/continental microphysical contrasts
500 in stratus. *Tellus B: Chemical and Physical Meteorology*, 54(1), 61-73. doi: 10
501 .3402/tellusb.v54i1.16648

Accepted Article